frontiers in Nanotechnology

TYPE Original Research
PUBLISHED 14 August 2026
DOI 10.3389/fnano.2026.1870683

OPEN ACCESS

EDITED BY
Themis Prodromakis,
University of Edinburgh, United Kingdom

REVIEWED BY
Dip Das,
University College London,
United Kingdom
Jakub Zdziebłowski,
Warsaw University of Technology, Poland

*CORRESPONDENCE
Peijia Yuan,
p.yuan@fz-juelich.de
Clemens Wittberg,
c.wittberg@fz-juelich.de

RECEIVED 01 May 2026
REVISED 16 June 2026
ACCEPTED 06 July 2026
PUBLISHED 14 August 2026

CITATION
Yuan P, Wittberg C, Deuermeier J, Elias Pereira M, Liu Y-P, Mueller DN, Kiazadeh A and Dittmann R (2026) Band-engineering in area-dependent InGaZnO(IGZO)-based memristive devices.
Front. Nanotechnol. 8:1870683.
doi: 10.3389/fnano.2026.1870683

Band-engineering in area-dependent InGaZnO(IGZO)-based memristive devices

Peijia Yuan[1]*, Clemens Wittberg[1]*, Jonas Deuermeier[2], Maria Elias Pereira[2], Yen-Po Liu[1], David N. Mueller[1], Asal Kiazadeh[2] and Regina Dittmann[1]

[1]Peter Grünberg Institut 7 (PGI-7), Forschungszentrum Jülich GmbH, Jülich, Germany, [2]CENIMAT|i3N, NOVA University Lisbon and CEMOP/UNINOVA, Caparica, Portugal

Area-dependent memristive devices based on the valence change mechanism are promising candidates for emerging analog and neuromorphic computing due to their intrinsic analog switching behavior and reduced variability. Among these, IGZO-based devices are particularly attractive owing to their potential for multifunctional applications, including optoelectronics and flexible electronics. However, systematic design strategies that directly link the material and interface properties to their device performance remain unexplored. In this work, we demonstrate that the switching polarity and electrical characteristics of IGZO-based memristive devices can be systematically tuned by modifying the top electrode. This control is shown to originate from changes in the band alignment and the resulting spatial electric field distribution across the device. To identify the governing interface and underlying transport mechanisms, we combine energy band diagram simulations with XPS-based band alignment measurements. Using this experimentally validated framework, the measured *I*–*V* characteristics are quantitatively reproduced within the Tsu–Esaki tunneling model. These results establish a consistent physical understanding of switching in IGZO-based devices and demonstrate that band engineering provides a powerful route to control both transport and switching behavior, enabling targeted optimization for large-scale analog and neuromorphic systems.

KEYWORDS
band alignment, band diagram, gradual switching, IGZO, memristive devices, Tsu-Esaki model, XPS

1 Introduction

The rapid advancement in artificial intelligence (AI) technology in recent years leads to a significantly increasing demand for accomplishing high workload tasks involving the processing of huge datasets. However, the performance and the energy bottleneck of the conventional von Neumann computing architecture arising from the physical separation of the processor and the memory limit the overall system efficiency (Von Neumann, 1993; Wulf and McKee, 1995; Backus, 1978). Therefore, the search for alternative computing approaches to overcome the memory wall is pressingly needed. Emerging computing paradigms, including neuromorphic computing and computing-in-memory, which co-locate computation and memory, provide a cost- and energy-efficient solution to this bottleneck (Sebastian et al., 2020). Redox-based resistive switching random access memory

(ReRAM) devices, also known as memristive devices, are widely investigated as promising building blocks for these novel computing concepts (Xia and Yang, 2019; Stavroulakis et al., 2025; Serb et al., 2016; Humood et al., 2025; Ielmini and Wong, 2018).

Typical two-terminal memristive devices consist of a metal-insulator-metal (MIM) structure, where a mixed ion-electron conducting material is sandwiched between two electrodes (Waser et al., 2009). The information can be stored using the resistance state of a device that is switched by applying an electrical bias. Various resistive switching mechanisms, including electrochemical metallization (ECM) (Chekol et al., 2022), valence change mechanism (VCM) (Aussen et al., 2023; Sarantopoulos et al., 2024), phase change memory (PCM) (Le Gallo and Sebastian, 2020), and complementary resistive switching (CRS) (Siemon et al., 2015) have been reported in literature. Among these concepts, VCM devices, including filamentary and area-dependent type devices, are particularly attractive due to their outstanding scalability and multi-level storage capability (Rao et al., 2023). Although filamentary type devices have been widely investigated for emerging computing applications (Bengel et al., 2021; Wang et al., 2025), their indispensable stochastic and abrupt electroforming step prior to regular switching introduces additional energy costs and high variability, thereby limiting their use in analog computing. In contrast, area-dependent switching devices exhibit an area-scaling behavior, where both the high-resistance state (HRS) and low-resistance state (LRS) scale with the device area, indicating that resistive switching is distributed across the entire device area. The gradual conductance change is attributed to the collective redistribution of oxygen vacancies or interstitial cations throughout the cross section, rather than to localized filament formation. As a result, localized stochastic effects are suppressed, enabling low device-to-device and cycle-to-cycle variability while maintaining gradual, analog switching behavior (Dittmann et al., 2021; Gutsche et al., 2021; Buczek et al., 2025).

Particularly promising in this context are IGZO-based area-dependent memristive devices, as amorphous IGZO can be deposited at room temperature in a fully CMOS BEOL–compatible process. Moreover, IGZO is widely employed in large-area electronics, particularly in thin-film transistor technologies for displays and memory, highlighting its industrial relevance (Kim et al., 2025). In addition to their compatibility with advanced integrated circuits, IGZO-based memristive devices offer strong potential for flexible electronics (Pereira et al., 2022), photosensing applications (Pereira et al., 2024; Hu et al., 2021), and memristive device-based cellular nonlinear network (M-CNN) implementations (Wang, 2025). However, despite the above-mentioned advantages for IGZO-based area-dependent memristive devices, systematic studies on rational device design controlling the switching characteristics and interface, as well as the current levels, are still lacking.

In this work, we present the design and fabrication of area-dependent IGZO-based memristive devices with engineered *I-V* characteristics and controllable current levels. All demonstrated device variants thereby exhibit gradual, synaptic-like plasticity, underscoring their suitability for neuromorphic computing applications. We demonstrate that modifying the top electrode (TE) material in a W/WO_x/IGZO/TE heterostructure systematically alters the switching polarity and, consequently, the overall device characteristics. The resulting variations in electrical behavior are elucidated through rigorous numerical simulations of the energy band diagrams, enabling clear identification of the interface governing resistive switching. The accuracy of the simulated band alignments is independently validated by XPS band alignment measurements at the WO_x/IGZO interface and the IGZO/Pt interface. Based on the extracted energy band profiles, the measured *I-V* characteristics are quantitatively described using the Tsu–Esaki tunneling model, explicitly accounting for the quasi-Fermi level distribution. The resulting fittings of the experimentally obtained *I-V* relations show remarkable agreement with both the experimentally determined band alignments from XPS and established literature values. Building on this understanding, the comprehensive energy-band analysis not only elucidates the fundamental switching mechanisms but also provides concrete design guidelines for future optimized device design for large-scale analog computing and neuromorphic systems.

2 Results and discussions

2.1 Area-dependent, gradual switching

The cross section of devices with a Ti/Au TE is schematically shown in Figure 1a. The quasi-static *I-V* characteristics of these devices exhibit clear hysteresis, as shown in Figure 1b. Devices were SET to a LRS by applying a negative voltage and were RESET to a HRS by applying a positive voltage. No current compliance is needed, as there is no electroforming process required prior to regular gradual switching. The initial resistance of devices with a Ti/Au TE is low, in the range of hundreds of Ohms to tens of kilo Ohms.

Each *I-V* curve in Figure 1b consists of five consecutive sweep cycles, demonstrating reproducible switching behavior. The corresponding HRS and LRS distributions extracted from the repeated sweep cycles are shown in the Supplementary Material. To further evaluate the reproducibility, extended 50-cycle measurements on one representative 50×50 μm^2 Ti/Au TE device, as well as measurements on ten 50×50 μm^2 Ti/Au TE devices, are also included in the Supplementary Material. These measurements confirm that the HRS and LRS remain clearly distinguishable, indicating low cycle-to-cycle and device-to-device variability.

Looking further at the *I-V* curves in Figure 1b we can see that the Ti/Au TE devices show gradual, area-dependent switching behavior, with the area scaling of device resistance extracted in Figure 1c. For ideal homogeneous area-dependent transport, the resistance is expected to scale inversely with the device area, corresponding to a slope of −1 in a double-logarithmic plot of resistance versus area. The initial resistance and LRS exhibit fitted slopes of approximately −1.09 and −1.03, respectively, which are close to the ideal value and confirm the area-dependent nature of the switching. In contrast, the HRS shows a steeper slope of approximately −1.84, indicating a stronger suppression of the off-current in smaller devices. This is also reflected in the increasing on-off ratio, defined as the resistance ratio (R_{OFF}/R_{ON}), with decreasing device size. A possible explanation of this observation is that smaller

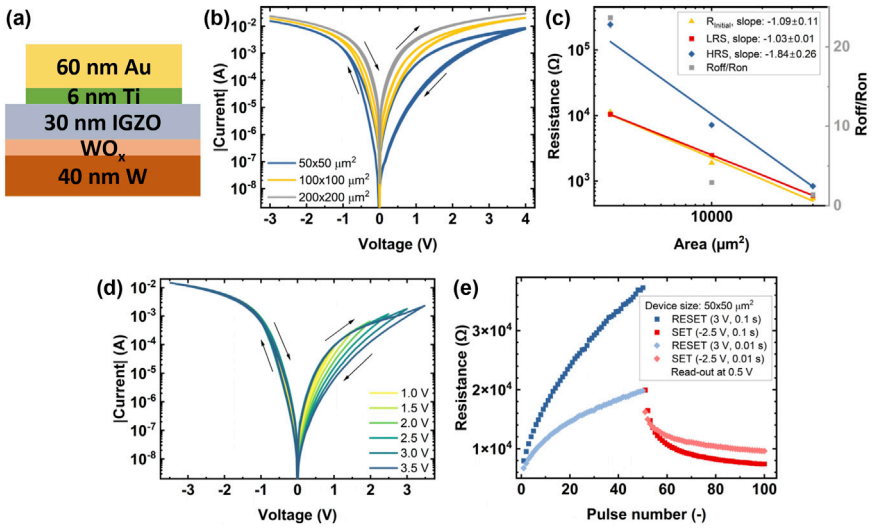

FIGURE 1
Electrical characterizations of W/WO_x/IGZO/Ti/Au memristive devices. **(a)** Schematic of the device stack. **(b)** Quasi-static *I-V* characteristics of devices with square side lengths of 50, 100, and 200 μm. Each curve consists of five consecutive sweep cycles. **(c)** Area-dependence of initial resistance, LRS, and HRS, and the on-off ratio read out at 0.5 V. The fitted slope values are shown in the legend box. **(d)** *I-V* characteristics of a 50 × 50 μm^2 device under different sweeping voltages between a maximum voltage of 1 V and 3.5 V. **(e)** Potentiation/depression measurements of a 50 × 50 μm^2 device. The applied SET/RESET voltage pulses are −2.5 V/3 V, and the widths of the voltage pulses are 0.1 s and 0.01 s. The read pulse is 0.5 V with a pulse width of 0.025 s. In the figure, SET (−3 V) and RESET (3 V) pulses are shown as red and blue points for 0.1 s, and as light red and light blue points for 0.01 s, respectively.

devices have a lower probability of containing local defect-rich regions or low-barrier leakage paths, leading to a disproportionately lower off-current and consequently a higher on-off ratio.

Figure 1d shows the *I-V* characteristics of a 50 × 50 μm^2 device under different sweeping voltages. There is no specifically defined SET or RESET voltage for gradual switching devices. Instead, devices could be switched within a voltage range over which clear hysteresis is observed, until dielectric breakdown occurs at around 4 V. The larger the applied voltage, the larger the on-off ratio, as further supported by the SET kinetics measurements shown in the Supplementary Material. Multiple intermediate resistance states could be reached, and they are well separated to reliably distinguish different states. This also verifies that these devices are suitable for multilevel switching.

Figure 1e shows exemplary potentiation/depression measurements on a 50 × 50 μm^2 device with a Ti/Au TE. Potentiation/depression measurements refer to conductance modulation induced by consecutive voltage pulses, where an increase or decrease in conductance corresponds to potentiation or depression, respectively. These measurements were performed by applying 50 identical voltage pulses to a device without switching it back to its initial state. A read pulse of 0.5 V at a pulse width of 0.025 s was applied after each SET or RESET pulse to read the device current. The applied SET/RESET voltage pulses were −2.5 V/3 V, and the widths of the voltage pulses were 0.1 s and 0.01 s. The device resistance gradually increases or decreases by the RESET or SET voltage pulses, demonstrating analog conductance modulation. The largest resistance change occurs at the first few pulses, as can be seen in the sparsity of the data points, indicating that the conductance update is state-dependent. This behavior is typical for VCM-type devices, where the pulse-induced resistance change is governed by the redistribution of oxygen defects near the active interface. Increasing the pulse width mainly improves the RESET/depression behavior, leading to a more gradual and uniform resistance increase. This can be attributed to the longer time available for ionic redistribution during each RESET pulse. In contrast, the SET/potentiation process remains less linear and shows a saturation tendency at later pulses. This likely results from the state-dependent accumulation of oxygen defects and the progressive reduction of the interfacial barrier as the device approaches the LRS, so that subsequent identical SET pulses induce smaller incremental resistance changes. In total, these results demonstrate the feasibility of multilevel analog switching in the IGZO-based devices.

By changing the TE to Pt, the devices exhibit distinctly different *I-V* characteristics. The device stack is schematically shown in Figure 2a. The corresponding quasi-static *I-V* characteristics and the area-dependence of devices are presented in Figures 2b,c, respectively. As for the Ti/Au TE devices, each *I-V* curve consists of five consecutive sweep cycles. The corresponding HRS and LRS current distributions extracted from the repeated sweep cycles are shown in the Supplementary Material. Additional extended cycling measurements on one representative Pt TE device are also provided in the Supplementary Material, confirming that the HRS and LRS remain clearly distinguishable over repeated cycling. This result confirms that these devices also exhibits clear gradual, area-dependent switching behavior. The initial resistance of devices with a Pt TE is in Giga Ohm range, which is significantly higher than that of devices with a Ti/Au TE and will be discussed in Subsection 2.3. To quantify the area dependence, the fitted slopes of

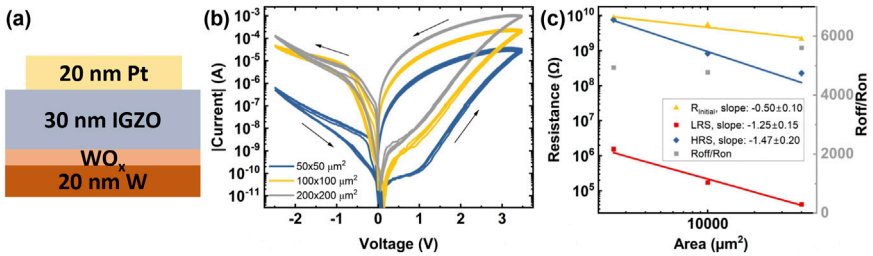

FIGURE 2
(a) Schematic of the W/WO_x/IGZO/Pt device stack. **(b)** Quasi-static *I-V* characteristics of devices with square side lengths of 50, 100, and 200 μm. Each curve consists of five consecutive sweep cycles. **(c)** Area-dependence of initial resistance, LRS, and HRS, and the on-off ratio read out at 0.5 V. The fitted slope values are shown in the legend box.

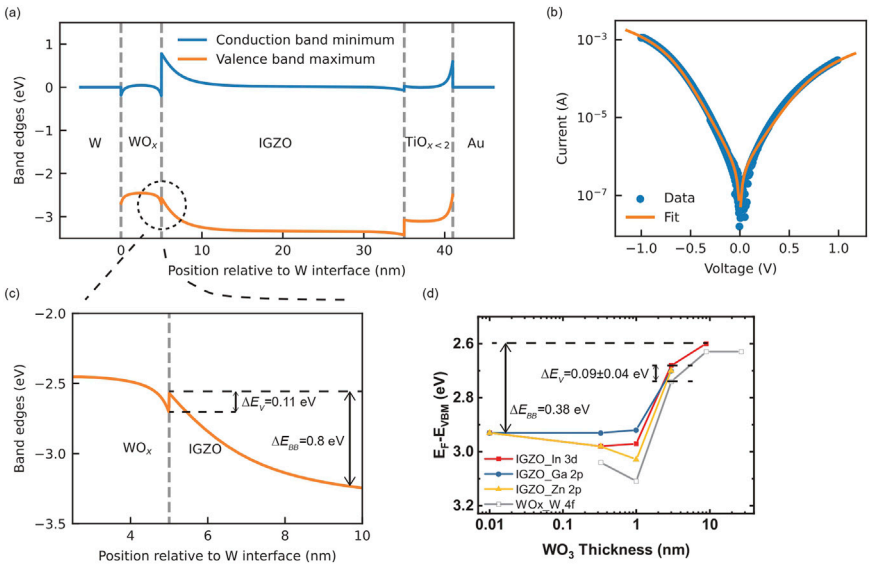

FIGURE 3
(a) Simulated band diagram for the Ti/Au TE devices using the parameters listed in Table 1, guided by the *I–V* fitting results. **(b)** Measured (blue symbols) and fitted (orange lines) *I–V* characteristics; the corresponding fitting parameters are summarized in Table 2. **(c)** Magnified view of the simulated valence band profile at the WO_x/IGZO interface. **(d)** Evolution of the valence band maximum relative to the Fermi level ($E_F - E_{VBM}$) as a function of WO_3 thickness, extracted from the XPS band alignment measurements shown in Figure 4.

the initial resistance, LRS, and HRS are approximately −0.50, −1.25, and −1.47, respectively. These deviations from the ideal −1 slope suggest that, although switching remains area-dependent, the effective active area does not scale perfectly with the nominal electrode area, likely due to local interface inhomogeneities and edge contributions. The deviation of the initial state is further attributed to the very low current level, which is close to the measurement resolution limit. The HRS also deviates from the ideal area dependence, consistent with the barrier-limited off-state transport. In addition, the on-off ratio is about two orders of magnitude higher than for Ti/Au TE devices. Most importantly, the switching polarity is reversed: Pt TE devices are RESET to the HRS under negative bias and SET to the LRS under positive bias. The pronounced differences in switching characteristics, particularly in current level, *I-V* curve shape, on-off ratio, and switching polarity are discussed in detail in the following subsections.

2.2 Band diagram simulation and energy band alignment XPS at WO_x/IGZO interface

To understand the device characteristics, and in particular the influence of the TE material on the *I-V* response and switching polarity, the band alignment across the full heterostructure is analyzed in the following sections. The band-edge profiles are obtained by solving the Poisson equation under equilibrium conditions, explicitly including Fermi level pinning effects as described in Section 3. Building on this band alignment analysis, we will demonstrate that the device characteristics of the Ti/Au TE devices are governed by the WO_x/IGZO interface in this section.

Examining the band diagram for the Ti/Au TE devices in Figure 3a, calculated using the parameters summarized in Table 1, it becomes evident that the Ti/Au electrode forms an effectively ohmic contact with the IGZO layer. This behavior arises from the partial oxidation of Ti, particularly at the

TABLE 1 Summary of the parameters used in the band alignment simulations shown in Figures 3a, 5a.

Parameter	Materials		
	WO_x	IGZO	$TiO_{x<2}$
Relative permittivity (ε_0)	4 (Kulikova et al., 2020)	10 (Marroun et al., 2019)	12 (Zhao et al., 2016)
Electron affinity (eV)	5.1†,‡ (Greiner et al., 2012; Marot et al., 2022)	4.2†,‡ (Marroun et al., 2019; Pereira, 2024)	4.1 (Yin et al., 2014)
Effective mass (m_e)	1.5 (Polaczek et al., 1994)	0.34 (Takagi et al., 2005)	1 (Huy et al., 2011)
Bandgap (eV)	2.6‡ (Greiner et al., 2012; Marot et al., 2022)	3.3‡ (Marroun et al., 2019)	3.1 (Yin et al., 2018)
Trap state depth shallow (eV)	-	0.2 ± 0.05 (Ide et al., 2019; Park et al., 2024)	0.3 ± 0.1 (Yin et al., 2018)
Trap state depth deep (eV)	-	0.8 ± 0.1 (Ide et al., 2019; Park et al., 2024)	-
Trap density Ti/Au TE ($\frac{1}{cm^3}$)	-	$5 \cdot 10^{19}$†	$5 \cdot 10^{20}$† (Carvalho et al., 2022)
Trap density Pt TE ($\frac{1}{cm^3}$)	-	$7 \cdot 10^{18}$†	-
Device/global parameters			
Workfunction W (eV)	4.6 (Kawano, 2008)		
Workfunction Au (eV)	5.3 (Kawano, 2008)		
Barrier height IGZO/Pt (eV)	0.37†,‡ (Flynn et al., 2018; Wilson et al., 2017)		

Parameters marked by † were tuned within the physically reasonable bounds to reproduce the experimental *I–V* characteristics (see Figures 3b, 5b), while parameters marked by ‡ were constrained by the XPS-derived band alignment.

interface with IGZO, leading to the formation of oxygen-deficient TiO_x. The presence of TiO_x reduces the conduction band offset relative to IGZO, thereby facilitating efficient electron injection and resulting in an ohmic-like contact (Carvalho et al., 2022). As a result, the TE/IGZO interface does not introduce a significant injection barrier and therefore cannot account for the observed exponential *I–V* characteristics or the switching behavior shown in Figures 3b, 1.

In contrast, inspection of the conduction band profile in Figure 3a reveals the formation of a pronounced, approximately quadratic barrier at the WO_x/IGZO interface. Notably, the associated electrostatic potential extends into the IGZO layer, giving rise to a Schottky-like depletion region, while the compensating charge accumulation is confined to an approximately 1 nm-thick region within the WO_x, analogous to conventional Schottky junctions. This distribution can be rationalized by the band alignment: the Fermi level of W lies within or close to the conduction band of the thin-film, high-work-function WO_x, resulting in a high electron concentration in the strongly doped WO_x. This high carrier density leads to the formation of a confined interfacial space-charge region within WO_x, which acts as a charge reservoir and enforces Fermi level pinning at the WO_x/IGZO interface. The resulting interface charge is screened by depletion of free electrons in the adjacent IGZO, leaving behind positively charged donor-like states attributed to oxygen defects. This establishes a space-charge region in IGZO and induces strong band bending analogous to that in conventional Schottky or *p–n* junctions. The resulting barrier therefore constitutes the dominant transport-limiting barrier governing the device characteristics.

To verify that the WO_x/IGZO barrier really constitutes the conduction-limiting element, the measured steady-state *I-V* characteristics shown in Figure 3b were quantitatively fitted. To disentangle the electronic transport characteristics from ionic switching effects, the steady-state *I-V* characteristics were obtained using pulsed measurements rather than conventional voltage sweeps. This approach minimizes changes in the ionic state during the measurement and thereby prevents unintended switching of the devices while acquiring the *I-V* characteristics Aussen et al. (2023). The current transport across the barrier is thereby described using the Tsu–Esaki tunneling formalism in combination with a constant series resistance (Funck et al., 2020; Gehring and Selberherr, 2006). In particular, the voltage-dependent quasi-Fermi level profile is explicitly taken into account, which is essential for accurately capturing electron transport in oxide-based Schottky barriers (see Section 3 and Supplementary Material). For the fitting procedure, the barrier is approximated by a quadratic potential, characterized by the effective barrier height Φ_B, the conduction band offset $\Delta\phi_n$, and the trap (or donor) concentration N, which together determine the barrier height, curvature, and effective width. In addition, two physically motivated parameters are introduced to account for Fermi level pinning and the bias-dependent modification of the quasi-Fermi level profile, as described in Section 3. These five parameters constitute the minimal, physically necessary, non-redundant set required to reproduce the measured *I-V* characteristics while avoiding overparameterization. The fitting is performed numerically under constrained parameter ranges to match the literature values, as summarized in Table 2. Additionally, the series resistance, which only limits the high-bias response, is fitted separately to account for resistive contributions outside the tunneling barrier. As shown in Figure 3b, the model quantitatively reproduces the experimental *I-V* characteristics over the entire voltage range. The extracted parameter set is subsequently used to refine the band bending calculations in Figure 3a, enabling a more accurate and self-consistent determination of the electrostatic potential across the

TABLE 2 Summary of the parameters used for fitting the *I–V* characteristics of the Ti/Au TE devices (Figure 3b) and Pt TE devices (Figure 5b), including the corresponding fitting bounds.

Parameter	Value Ti/Au TE	Value Pt TE	Bounds
Barrier height Φ_B (eV)	0.9	0.92	[0.5, 1.3] (Marot et al., 2022; Marroun et al., 2019)
Conduction band offset $\Delta\phi_n$ (eV)	0.23	0.3	[0.01, 0.5] (Pereira, 2024)
Trap concentration N_D $(\frac{1}{cm^3})$	$5 \cdot 10^{19}$	$7 \cdot 10^{18}$	$(1 \cdot 10^{17}, 5 \cdot 10^{21})$
Fermi level pinning factor S_{FL-pin} (1)	0.7	0.65	[0.3, 1] (Flynn et al., 2018; Wilson et al., 2017)
Tunneling energy scaling factor R_{QFL} (1)	0.5	0.5	[0.3,1]
Series resistance R (Ω)	200	6000	-

heterostructure. This agreement strongly supports the conclusion that the WO_x/IGZO interface barrier governs the dominant transport mechanism in the device.

However, while the calculated band profile can self-consistently reproduce the observed *I-V* characteristics, this agreement alone does not constitute direct proof that a transport-limiting barrier is located at the interface. To experimentally validate the simulated band alignment, we therefore performed energy band alignment measurements using XPS. The band alignment at the interfaces was determined following the established methodology described in (Waldrop et al., 1985; Klein, 2012). The underlying principle is that, although the valence bands of the substrate and film overlap when they are stacked, their core levels remain spectroscopically distinct and can thus serve as stable internal energy references. A stepwise deposition approach was employed, with XPS spectra recorded after each deposition step. For the bare substrate and the thick film limit, the core-level-to-valence-band maximum separations are defined as material-specific constants. By referencing the measured core-level binding energies to these offsets, the evolution of the valence band position relative to the Fermi level can be tracked during film growth, enabling extraction of the valence band offset ΔE_V from the regime where both materials exhibit a common potential shift. In addition, band bending ΔE_{BB} is obtained from the thickness-dependent evolution of the substrate core-level binding energies. Once the valence band offset and bandgap values are determined, the conduction band offset can be derived, allowing reconstruction of the full band alignment diagram, thereby enabling direct experimental verification of the transport barrier inferred from electrical measurements.

In this work, we explicitly performed an *in situ* step-by-step deposition of WO_3 on IGZO. A 30 nm IGZO layer was first deposited on a 30 nm Pt-coated 430 nm SiO_2/Si substrate. Subsequently, WO_3 was sputtered in incremental thickness steps, with XPS core-level spectra recorded after each deposition step without breaking vacuum. In addition, reference valence-band spectra of bulk IGZO and bulk WO_3 were acquired from the same samples. The measured XPS core level spectra of W 4f, In $3d_{5/2}$, Ga $2p_{3/2}$, Zn $2p_{3/2}$, and the valence bands of bulk IGZO and WO_3 are shown in Figure 4. As the WO_3 thickness increases, the In, Ga, and Zn core-level signals gradually decrease in intensity, while the W 4f signal correspondingly increases. Once the WO_3 thickness exceeds the XPS information depth, the IGZO core-level signals are fully attenuated. At a WO_3 thickness of 9 nm, only the In 3d signal remains slightly detectable among the IGZO-related core levels,

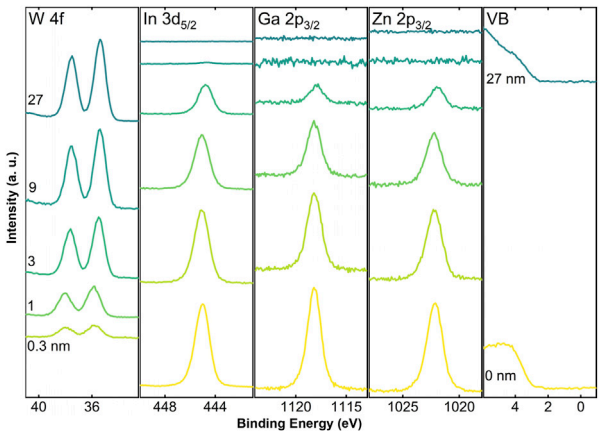

FIGURE 4
Sequential *in situ* XPS spectra of the WO_3/IGZO interface recorded after incremental WO_3 deposition steps. The WO_3 thickness is indicated in nm. Core levels of W 4f, In $3d_{5/2}$, Ga $2p_{3/2}$, Zn $2p_{3/2}$, and the valence bands of bulk IGZO and WO_3 are displayed.

consistent with its larger inelastic mean free path (IMFP) compared to Ga and Zn core levels (Shinotsuka et al., 2015). Importantly, the line shapes of all core levels remain unchanged throughout the deposition, indicating the absence of chemical shifts and thus preservation of chemical integrity at the interface. The valence band maxima (VBM) of IGZO and WO_3 were determined using linear extrapolation of the leading edge. By referencing the corresponding core-level to VBM offsets, the evolution of the valence band position relative to the Fermi level as a function of WO_3 thickness is obtained, as shown in Figure 3d. From this analysis, a valence band offset of 0.09 ± 0.04 eV is extracted. In addition, a band bending of 0.38 eV is determined for IGZO from the thickness-dependent shift of the substrate core levels.

Comparison between the simulated valence band profile at the WO_3/IGZO interface in Figure 3c and the experimentally determined band alignment in Figure 3d shows good overall agreement. In particular, the simulated valence band offset of 0.11 eV is in good agreement with the experimentally extracted value. The experimentally observed band bending of ≈ 0.38 eV, follows the same direction as the simulation, although with reduced magnitude, which is most likely attributed to a lower oxygen defect concentration during the XPS band alignment experiment compared to the device structure, where Ti-induced

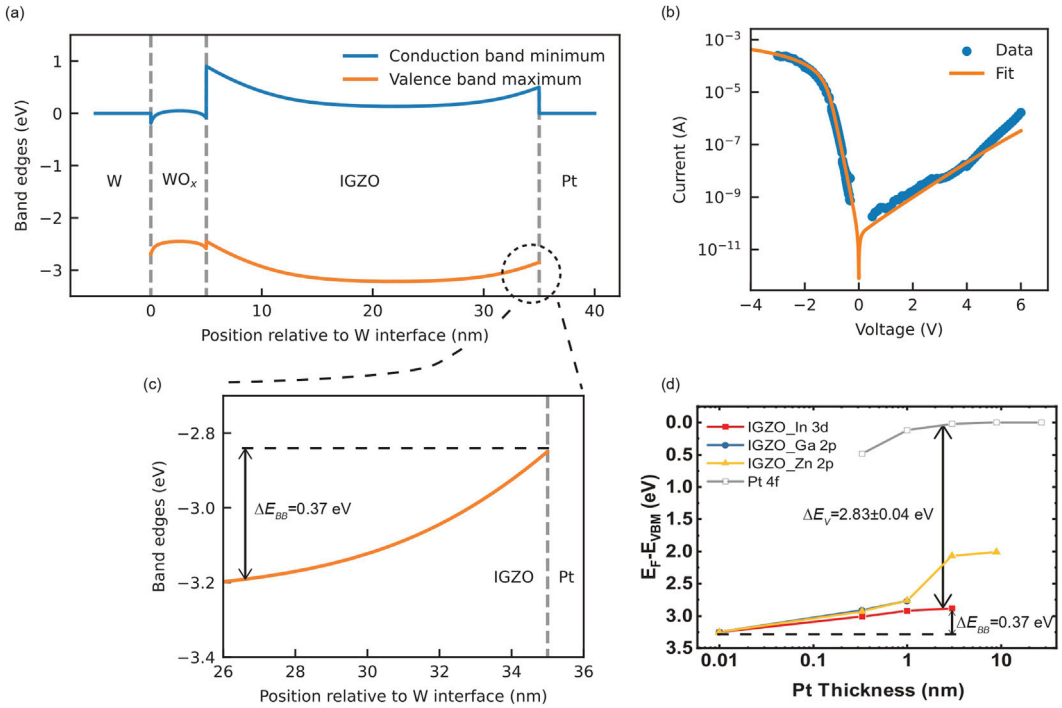

FIGURE 5
(a) Simulated band diagram for the Pt TE devices using the parameters listed in Table 1, guided by the I–V fitting results. **(b)** Measured (blue symbols) and fitted (orange lines) I–V characteristics; the corresponding fitting parameters are summarized in Table 2. **(c)** Magnified view of the simulated valence band profile at the Pt/IGZO interface. **(d)** Evolution of the valence band maximum relative to the Fermi level (EF − EVBM) as a function of Pt thickness, extracted from the XPS band alignment measurements shown in Figure 6.

reduction of IGZO is present as discussed earlier. This agreement provides strong validation that the simulated band alignment captures the WO_x/IGZO interface energetics. Consequently, this combined experimental–theoretical consistency strongly supports the conclusion that the WO_x/IGZO interface-induced barrier constitutes the dominant conduction-limiting barrier governing the Ti/Au TE device characteristics.

2.3 Top electrode/IGZO interface engineering

To understand the influence of the top electrode and to derive design strategies via band engineering, we now analyze the Pt TE devices with particular emphasis on the role of the electrode material. In contrast to the Ti/Au system, where the reactive Ti layer induces the formation of an interfacial TiO_x and thereby alters the band alignment, Pt represents a chemically inert electrode that does not form a conductive interfacial oxide. Owing to its higher work function, Pt would nominally be expected to form a Schottky barrier at the IGZO interface; however, this behavior can be significantly modified by Fermi level pinning effects, which are known to depend sensitively on the deposition conditions and defect landscape of both IGZO and Pt (Flynn et al., 2018; Wilson et al., 2017). As such, the Pt TE devices provide a model system to disentangle intrinsic band alignment tendencies from pinning-induced deviations and chemically induced interface modifications.

Analogous to the Ti/Au TE devices, the device characteristics of the Pt TE structures are analyzed in terms of the corresponding band bending. In contrast to the Ti/Au case, however, the barrier height of a potential Schottky barrier at the IGZO/Pt interface cannot be defined *a priori* due to these pronounced Fermi level pinning effects (Flynn et al., 2018; Wilson et al., 2017). Consequently, reported barrier heights span a wide range, typically between 0.2 eV and 1.2 eV. Hence to obtain a physically consistent band diagram, as depicted in Figure 5a, the measured *I–V* characteristics were first fitted using the Tsu–Esaki tunneling model again in combination with a constant series resistance. In contrast to the Ti/Au devices, charge transport was modeled by considering two oppositely biased Schottky barriers located at the WO_x/IGZO and IGZO/Pt interfaces, respectively, which were treated as independent for the purpose of fitting. Performing these fits while keeping all parameters at the WO_x/IGZO interface identical to the previous analysis—except for the doping concentration and the corresponding conduction band offset—yields results that are only consistent if the IGZO/Pt interface behaves effectively as an ohmic contact similar to the results presented by (Schultz et al., 2018). This conclusion is further supported by the experimental observation that lower currents are measured when the IGZO/Pt interface is forward biased compared to reverse bias, which is inconsistent with the rectifying behavior expected for a Schottky contact at the IGZO/Pt interface where higher forward currents would be expected.

However, also in this case, the self-consistent agreement between the fitting results, the observed *I–V* characteristics, and the behavior of the Ti/Au devices does not constitute direct proof that the IGZO/Pt interface behaves as an ohmic contact. To experimentally validate the band alignment and directly probe

the nature of the IGZO/Pt barrier, we therefore performed energy band alignment measurements using XPS. The XPS spectra of In $3d_{5/2}$, Ga $2p_{3/2}$, Zn $2p_{3/2}$, Pt 4f, as well as the valence band of bulk IGZO and the Fermi edge of Pt, were recorded during a stepwise *ex situ* deposition of Pt on IGZO, as shown in Figure 6. Based on their IMFP values, the Ga 2p and Zn 2p signals are expected to attenuate more rapidly than the In 3d signal (Shinotsuka et al., 2015). However, at Pt thicknesses of 3 nm and 9 nm, the Zn $2p_{3/2}$ peak remains visible, whereas the Ga $2p_{3/2}$ signal is no longer detectable. In addition, the Zn $2p_{3/2}$ peak shifts toward lower binding energy, indicating that a small fraction of Zn diffuses into and alloys with the Pt layer. Quantitative analysis yields a Zn concentration of approximately 1.8 at% at 3 nm Pt and 0.9 at% at 9 nm Pt. Such low Zn incorporation is expected to have a negligible influence on the Pt 4f binding energy (Galloway et al., 2009). At very low Pt thicknesses (0.3 nm and 1 nm), a slight positive shift in the Pt 4f binding energy is observed. This deviation from bulk values is attributed to the non-continuous nature of the film at these thicknesses, where the formation of isolated islands leads to reduced electronic screening and localized charging effects (Isomura et al., 2010; Dobierzewska-Mozrzymas et al., 2001). The evolution of the valence band position relative to the Fermi level as a function of Pt thickness is shown in Figure 5d. In this analysis, a valence band offset of 2.83 ± 0.04 eV and a band bending of 0.37 eV in IGZO are extracted. Comparison with the simulated band diagram shown in Figure 5c reveals very good agreement, with a simulated band bending also of approximately 0.37 eV. The small magnitude of the observed band bending indicates that the Fermi level is strongly pinned at the IGZO/Pt interface. This interpretation is further supported by complementary measurements presented in the Supplementary Material, where stepwise deposition of IGZO on Pt reveals a pronounced reduced component in the In 3d spectrum at the interface. This can be attributed to the same strong Fermi level pinning mechanism (Flynn et al., 2018; Wilson et al., 2017), leading to a very small barrier and hence ohmic conduction across this interface.

Based on this result, the question arises as to why the *I–V* characteristics differ significantly, despite both top electrode contacts exhibiting effectively ohmic behavior and the same WO_x/IGZO interface acting as the conduction-limiting barrier. To address this, the fitting parameters summarized in Table 1, corresponding to the fit shown in Figure 5b, are examined. While the extracted barrier height at the WO_x/IGZO interface, as well as the parameters describing Fermi level pinning and the quasi-Fermi level profile, remain unchanged within fitting uncertainty compared to the Ti/Au TE case, the doping concentration in IGZO is consistently found to be approximately one order of magnitude lower. This reduction can be attributed to the absence of a reactive Ti layer, which in the Ti/Au devices induces partial reduction of IGZO and promotes the formation of oxygen defects. The reduced doping concentration increases the spatial extent of the depletion region by a factor of ≈ 2.7, thereby enlarging the effective tunneling distance. Since the transmission probability depends exponentially on the barrier width (cf. Equation 8), this large increase in depletion width leads to a substantial reduction in current for the Pt TE devices compared to the Ti/Au TE devices explaining the orders of magnitude different resistances observed in Figures 1c, 2c. In particular this becomes obvious for the initial pristine resistance

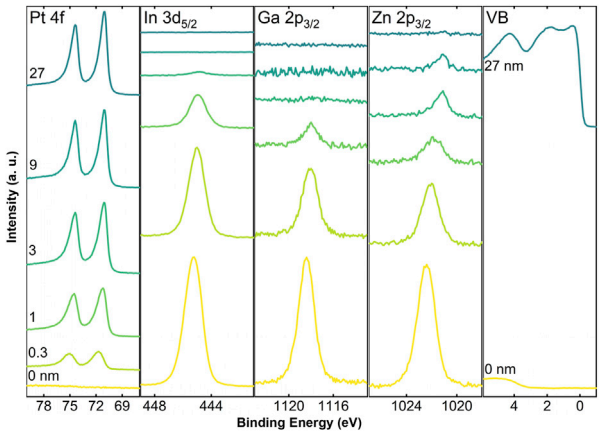

FIGURE 6
Sequential ex situ XPS spectra of the IGZO/Pt interface recorded after incremental Pt deposition steps. The Pt thickness is indicated in nm. Core levels of Pt 4f, In 3d5/2, Ga 2p3/2, Zn 2p3/2, the valence band of bulk IGZO, and the Fermi edge of Pt are displayed.

where the resistance differs by seven orders of magnitude before any voltage induced changes of the oxygen defect concentration (c.f. Figures 1c, 2c).

In addition, also the fitted conduction band offset increases slightly to $\Delta\phi_n \approx 0.3$ eV, consistent with a reduced oxygen defect concentration and prior reports (Pereira, 2024). In agreement with this picture, an approximately one order of magnitude higher series resistance—primarily attributed to the ohmic electron conduction through the bulk IGZO layer—is observed compared to the Ti/Au devices.

Consequently, the modified *I–V* characteristics of the Pt TE devices can be consistently explained by the combined effect of reduced doping and, correspondingly, a slightly increased energy separation between the conduction band and the Fermi level. Both effects contribute to an increased effective barrier width. This thicker barrier not only quantitatively reproduces the measured transport behavior but also provides a consistent physical explanation for the reduced current levels, enhanced rectification, and increased on–off ratio in the Pt TE devices. The more pronounced rectification observed in Figures 2b, 5b arises from the strong exponential dependence of the transmission probability on barrier width in the Tsu–Esaki framework (c.f. Equation 8): Under a reverse biased WO_x/IGZO barrier, the increased barrier width strongly suppresses tunneling, whereas a forward bias effectively lowers and narrows the barrier, enabling higher current flow (Gehring and Selberherr, 2006). Hence the currents under a reverse bias are up to seven orders of magnitude smaller compared to the forward bias as observed in Figure 5b. In contrast, for thinner barriers, this exponential suppression is less pronounced and tunneling can happen close to the Fermi level, allowing significant tunneling in both bias directions and thus a more symmetric *I–V* relation. This explains also why the *I–V* characteristics for the leakier Ti/Au TE devices are much more symmetric as seen in Figures 1b, 3b.

Apart from the observed rectification, the same strong dependence of the tunneling probability on barrier width also explains the approximately two orders of magnitude larger switching window observed for the Pt TE devices compared to

the Ti/Au TE devices under a reverse biased WO_x/IGZO barrier, as shown in Figures 1b, 2b. Since the tunneling current depends exponentially on the barrier width, changes in the oxygen defect concentration have a much stronger impact on the current flowing through the wider and more resistive barriers of the Pt TE devices than through the already leakier and thinner barriers of the Ti/Au TE devices, particularly under reverse bias (Gehring and Selberherr, 2006). This behavior is further illustrated by the static *I-V* characteristics calculated for different oxygen defect concentrations and presented in the Supplementary Material. The corresponding defect concentrations were extracted from the SET-kinetics measurements discussed therein. The simulations show that the modulation of the steady-state *I-V* characteristics caused by changes in the oxygen defect concentration is substantially larger for the Pt TE devices than for the Ti/Au TE devices. Consequently, the experimentally observed hysteresis window opens much more strongly for the Pt TE devices, particularly for positive bias applied to the TE. Furthermore, the simulations also explain the slightly larger hysteresis opening observed for negative bias applied to the top electrode in the Pt TE devices. Overall, the calculated steady-state *I-V* characteristics for different oxygen defect concentrations reproduce the main features of the experimentally observed hysteresis behavior and provide additional support for the electronic model and proposed switching mechanism.

In summary these findings demonstrate that band engineering offers a powerful approach for tailoring the electronic transport and resistive switching properties of oxide heterostructure devices through precise control of the effective tunneling barrier and its defect-mediated modulation.

After understanding the current transport in both devices and establishing that in both cases the same WO_x/IGZO interface constitutes the conduction-limiting barrier, the question arises as to why the switching polarity differs. As shown in Figure 1a and the SET-kinetics measurements presented in the Supplementary Material, the Ti/Au TE devices exhibit SET under negative bias and RESET under positive bias applied to the TE. Given that the WO_x/IGZO interface dominates the voltage drop, switching must originate from field-driven processes occurring in its vicinity. This is supported by the observation that the potential primarily drops across the WO_x/IGZO barrier within the first $\lesssim 10$ nm of the IGZO layer also under applied biases, as shown in the Supplementary Material. Within this framework, the Ti/Au switching behavior can be attributed to the migration of oxygen defects between the WO_x and IGZO layers, which modulates the effective barrier width and thereby the tunneling current. This explanation is thereby consistent with the electronic model as shown in the Supplementary Material and with related oxide systems explaining the observed switching polarity (Cooper et al., 2017; Baeumer et al., 2016; Funck et al., 2020; Carvalho et al., 2022).

In contrast, the Pt TE devices exhibit reversed switching polarity, which can be understood from a modified electric field distribution arising from the increased effective barrier width. In this case, the voltage drop is not confined to the immediate vicinity of the WO_x/IGZO interface but can extend across the entire IGZO layer under reverse bias (i.e., positive bias applied to the top electrode), as supported by the band diagrams in Figures 3a, 5a and the Supplementary Material. This extended field enables defect drift throughout the IGZO layer and establishes a spatially distributed driving force for oxygen defect migration. In addition, it may facilitate oxygen exchange processes at the Pt interface, particularly at grain boundaries (Cooper et al., 2017; Baeumer et al., 2016; Hellwig et al., 2024; Zurhelle et al., 2022). These modified oxygen migration pathways are further supported by the observation that, in contrast to the Ti/Au devices, the ionized oxygen vacancies are less localized in the immediate vicinity of the interface. This greater spatial delocalization promotes bulk-mediated vacancy transport within IGZO and facilitates oxygen exchange with the Pt electrode, making these processes more favorable than the localized exchange at the WO_x/IGZO interface. Within this framework, the observed switching polarity can be consistently explained: a positive bias applied to the TE drives oxygen vacancies toward the WO_x/IGZO interface, increasing the charge density in the space-charge region and thereby reducing the effective barrier width as shown in the Supplementary material. Hence this migration process results in a SET transition. Conversely, applying a negative bias extracts vacancies from the interfacial region, reducing the space-charge density, increasing the barrier width, and thus inducing a RESET transition.

Consequently, the reversal of switching polarity in the Pt TE devices can be consistently explained by the transition from a localized interfacial field-driven defect modulation (Ti/Au) to a distributed field-driven defect transport regime possibly also enabling the oxygen exchange with the Pt TE. These results highlight that band engineering enables systematic control not only over the charge carrier transport but also over both switching dynamics and polarity through deliberate modulation of the electric field distribution within the device.

3 Experimental

3.1 Fabrication of IGZO-based memrsitive devices

The IGZO-based memristive devices discussed in this work can be classified into two groups based on their top electrode (TE) used, either Ti/Au or Pt, as schematically shown in Figures 1a, 2a. The sample substrates were 10×10 mm^2 Si with a 430 nm thermal SiO_2 layer. For devices with a Ti/Au TE, a 40 nm tungsten layer was deposited as the bottom electrode (BE) using radio-frequency magnetron sputtering. Then, the layer was oxidized in an oxygen plasma atmosphere in a plasma asher at 200 sccm, 300 W for 30 min with a Faraday cage to form a thin WO_x interfacial layer. Afterwards, a 30 nm amorphous IGZO layer was deposited by pulsed laser deposition (PLD) under an oxygen pressure of 0.108 mbar, at room temperature, and a laser fluence of 2.45 J/cm^2. The IGZO target composition followed a 2:1:1 atomic ratio of In_2O_3:Ga_2O_3:ZnO. Finally, a Ti/Au (6 nm/60 nm) TE was deposited by e-beam evaporation. Devices with a Pt TE consist of a 20 nm W BE following an oxygen plasma treatment, a 30 nm IGZO layer, and a 20 nm Pt deposited by e-beam evaporation. The deposition parameters for W and IGZO and the oxygen plasma treatment parameters were identical as for devices with Ti/Au TE. Samples were patterned by a shadow mask with an array of square sets with square side lengths of 10, 50, 100, and 200 μm during the TE evaporation process.

3.2 Electrical characterization

To characterize the electrical properties of these devices, samples were glued onto a 25.4 × 25.4 mm^2 carrier wafer with Pt pads and connected with one Pt pad by an aluminum wire containing 1% Si with a diameter of 25 μm. Quasi-static *I-V* characteristics were measured using a Keithley 2611A source measurement unit and a PM5 probe station with two micromanipulators. Two gold-coated tungsten probe tips were used to contact the TE and BE of the devices. The voltage was applied to the TE, and the BE was grounded. All quasi-static *I-V* sweep measurements were performed with a maximal current compliance of 100 mA, a voltage step width of 30 mV, and a hold time before measuring of 20 m. Pulsed measurements were carried out using a Keithley 4200A SCS pulsed measurement unit in conjunction with a PM5 probe station. A trapezoidal voltage pulse profile was employed, with rise and fall times of $1 \cdot 10^{-7}$ s, selected to be significantly shorter than the duration of the steady-state plateau of $1 \cdot 10^{-2}$ s in order to minimize transient effects and ensure stable current acquisition during the constant bias interval. The sampling frequency was set to $1 \cdot 10^{5}$ s^{-1}, and the current measurement range was varied between $1 \cdot 10^{-7}$ A and $1 \cdot 10^{-5}$ A to optimize sensitivity across different conduction regimes.

3.3 X-ray photoelectron spectroscopy

X-ray photoelectron spectroscopy (XPS) measurements were performed using a VersaProbe PHI 5000 instrument with an Al Kα x-ray source with a photon energy of 1486.7 eV, and a dual beam charge neutralization system. For *in situ* band alignment measurements, samples were transferred from the PLD chamber to the XPS chamber through an ultra-high vacuum tunnel to avoid oxidation or contamination of the measured interface. Samples were glued on an omicron plate using silver paste, and the sample edges were additionally covered with silver paste to suppress charging and to ensure good electrical grounding during the spectroscopy measurements. Both the electron neutralizer and the ion neutralizer were off, as the sample was already well grounded. The binding energy scale was calibrated by measuring the Fermi edge of a sputter-cleaned Au foil, as shown in Supplementary Figure S1.

3.4 Band alignment simulation

To rationalize the device *I-V* characteristics and resistive switching behavior, the band alignment across the full heterostructure was computed in order to identify the conduction-limiting barriers governing charge transport. The band alignment calculations were performed using our in-house simulation code, which is publicly available in the Jülich DATA repository (Clemens, 2026).

Since the conduction band minimum (CBM) relative to the Fermi level E_F is given by

$$E_c(x) = -e\phi(x) + e\chi(x) \tag{1}$$

where $\chi(x)$ denotes the (generally position-dependent) electron affinity and $\phi(x)$ the electrostatic potential referenced to the vacuum level, determining the CBM reduces to solving for the electrostatic potential throughout the heterostructure. Accordingly, the Poisson equation

$$\frac{d^2\phi(x)}{dx^2} = -\frac{\rho(x)}{\varepsilon} \tag{2}$$

is solved, where ε is the permittivity and $\rho(x)$ the position-dependent charge density.

The total charge density comprises contributions from free carriers in both conduction and valence bands. Within the parabolic band approximation, the corresponding densities of states are expressed as

$$D_{C,V}(E,x) = \frac{1}{2\pi^2}\left(\frac{2m^*_{e,h}}{\hbar^2}\right)^{3/2}\sqrt{\pm E \mp E_{c,v}(x)} \tag{3}$$

where $m^*_{e,h}$ are the effective masses of electrons and holes, respectively, E is the carrier energy referenced to the Fermi level, and $E_{c,v}(x)$ denote the CBM and valence band maximum (VBM). The latter is given by $E_v(x) = E_c(x) - E_g$, where E_g is the bandgap. Carrier occupations follow Fermi–Dirac statistics, yielding

$$\rho_{c,v-band}(x) = \mp e\int_{-\infty}^{\infty} dE\; D_{C,V}(E,x)\frac{1}{1+\exp\left(\pm\frac{E-E_F}{k_BT}\right)} \tag{4}$$

where the integrals extend over all energetically accessible states in the respective bands. In addition to band carriers, charge contributions from donor-like trap states, attributed to oxygen defects, are included. Their contribution is given by

$$\rho_{trap}(x) = e\int_0^{E_g} d\phi_t\; D(\phi_t,x)\frac{1}{1+2\exp\left(-\frac{E_c(x)-\phi_t-E_F}{k_BT}\right)}, \tag{5}$$

where $D(\phi_t, x)$ is the trap density of states as a function of position x and trap depth ϕ_t —here assumed to be Gaussian. The occupation again follows Fermi–Dirac statistics now including spin degeneracy and is integrated over all trap energies within the bandgap.

Combining all contributions, the Poisson equation becomes

$$\frac{d^2\phi(x)}{dx^2} = -\frac{\rho_{c-band}(x) + \rho_{v-band}(x) + \rho_{trap}(x)}{\varepsilon} \tag{6}$$

which must be solved self-consistently to obtain the spatially resolved electrostatic potential. Due to the nonlinear and implicit dependence of the charge density on $\phi(x)$—through its coupling to the CBM (cf. Equation 1) and the Fermi–Dirac distributions—closed-form analytical solutions are not accessible, necessitating a numerical treatment.

In this work, the resulting boundary value problem is solved using a finite-difference approach implemented via the `solve_bvp` routine from the `scipy.integrate` module (Virtanen et al., 2020). Particular care is taken to enforce continuity of the electric displacement field εE across material interfaces, including under applied bias and in the presence of interfacial charge contributions, which can give rise to non-negligible Fermi level pinning (Sze and Ng, 2006). The Dirichlet boundary conditions account for both the work function difference between the top and bottom electrodes and the externally applied bias voltage, under the assumption of ideal metal contacts. All numerical and physical simulation parameters are summarized in Table 1.

3.5 Fittings of the current-voltage relation.

To obtain physically consistent parameters for the band bending calculations, *I-V* fitting was performed based on pulsed *I-V* measurements, thereby isolating purely electronic transport contributions and suppressing ionic effects (Aussen et al., 2023). Guided by preliminary band diagram estimates using literature parameters, electron transport is assumed to be limited by barriers forming at the interfaces. Under this assumption, the current transport can be described within the Tsu–Esaki tunneling formalism, as detailed by Funck et al. (2020); Gehring and Selberherr (2006). Here the tunneling current density is given by

$$j = \frac{A^\star}{k_B^2}\int_{E_{\min}}^{E_{\max}} T\left(E_y\right)\cdot N\left(E_y,T\right)\,dE_y, \tag{7}$$

where $A^\star = \frac{4\pi m_{\mathrm{eff}} e k_B^2}{h^3}$ denotes the effective Richardson constant, $T(E_y)$ the transmission probability, $N(E_y,T)$ the supply function, and E_y the transverse tunneling energy. Within the WKB approximation, the transmission function for electrons tunneling between the classical turning points x_i and x_t, defined by $E_c(x_{i,t}) = E_y$, is given by

$$T\left(E_y\right) = \exp\left(-\frac{2}{\hbar}\int_{x_i}^{x_t} dx\sqrt{2m_t^\star\left[E_c(x)-E_y\right]}\right), \tag{8}$$

where m_t' denotes the tunneling effective mass. The corresponding supply function reads

$$N\left(E_y,T\right) = k_B T\ln\left[\frac{1+\exp\left(-\frac{E_y-E_F+eV}{k_BT}\right)}{1+\exp\left(-\frac{E_y-E_F}{k_BT}\right)}\right], \tag{9}$$

where V denotes the applied bias voltage. Assuming, as a good first-order approximation (Funck et al., 2020), quadratic barrier profiles (coming from a homogeneous charge distribution inside the barrier), fitting the calculated *I-V* characteristics to the experimental data enables extraction of the barrier height Φ_B, the effective barrier curvature (related to the trap or doping concentration N_D), and the conduction band offset $\Delta\phi_n$.

However, the present system deviates from the ideal (Schottky) barrier description due to Fermi level pinning and a spatially varying quasi-Fermi level, arising from thermally activated and tunneling-mediated exchange between trap states and extended band states. Fermi level pinning is well known in IGZO-based Schottky barriers, particularly under oxygen-deficient conditions as assumed here (Flynn et al., 2018; Wilson et al., 2017), where oxygen-related defect states and interface states significantly reduce the effective barrier modulation. In addition, in nm-scale oxide (Schottky) barrier systems, enhanced tunneling exchange between the bands and energetically distributed trap states leads to an alignment of the quasi-Fermi level in the oxide with the Fermi level on the other side of the barrier near the interface. This effect is a direct consequence of strong interfacial coupling through enhanced tunneling exchange and can be rigorously derived from static quasi-Fermi level simulations as shown in the supplement. As a result, the upper integration limit $E_{\max}$ in Equation 7 is determined by the bias-dependent quasi-Fermi level profile, since thermally activated carriers at higher energies near the interface do not contribute to the net current due to the alignment of the quasi-Fermi levels on both sides of the barrier.

To account for these non-idealities, the model is extended by introducing (i) an effective Fermi level pinning factor $S_{\mathrm{FL-pin}}$ (Sze and Ng, 2006), which reduces the fraction of the change in built-in potential relative to the applied bias according to

$$\frac{\partial}{\partial V}\left(\Phi_B - \Delta\phi_n - V\right) = S_{\mathrm{FL-pin}} \tag{10}$$

and (ii) an additional scaling factor describing the bias dependence of the maximum accessible tunneling energy. Based on rigorous quasi-Fermi level simulations shown in the supplement we thereby assume that also the voltage dependence of the upper integration limit is linear leading to

$$\frac{\partial E_{\max}}{\partial V} = R_{\mathrm{QFL}}, \tag{11}$$

with the tunneling energy scaling factor R_{QFL}.

Including these extensions, the measured *I-V* characteristics were fitted using the model described above, employing the `curve_fit` routine from the `scipy.optimize` module with all parameters being restricted to a physically reasonable range (Virtanen et al., 2020). The fitting procedure yields the Schottky barrier height Φ_B, effective doping (or trap) concentration N_D, Fermi level offset $\Delta\phi_n$, Fermi level pinning factor $S_{\mathrm{FL-pin}}$, and tunneling energy scaling factor R_{QFL}. All numerical and physical fitting parameter constraints are summarized for each fitting individually in Table 1.

4 Conclusion

In summary, IGZO-based memristive devices with area-dependent switching characteristics were fabricated and systematically investigated. The devices exhibit gradual, analog switching and synaptic-like plasticity, highlighting their potential for neuromorphic computing applications. In addition, the operating current range can be tuned via device scaling, providing an additional degree of freedom for application-specific optimization.

Comprehensive band diagram analysis reveals the formation of a conduction-limiting barrier at the WO_x/IGZO interface, which governs charge transport in both device configurations. The excellent agreement between simulated band alignment and XPS-derived measurements establishes a quantitative and experimentally validated energy-band description of the full heterostructure.

By varying the top electrode material, both switching polarity and electrical characteristics can be systematically engineered while preserving the intrinsic gradual and area-dependent switching behavior. This behavior is consistently explained by electrode-induced modifications of the band alignment and the resulting electric field distribution across the device.

Overall, these results provide a unified physical understanding of both current transport and switching dynamics, and establish band engineering as a practical and transferable design principle for optimizing IGZO-based memristive devices. This enables rational

control of device functionality for scalable analog computing and neuromorphic applications.

Data availability statement

The original contributions presented in the study are included in the article/Supplementary Material. The simulation code used for the band diagram calculations is publicly available at (https://iffgit.fz-juelich.de/pgi-7/band-alignment-calculations) and archived under DOI: (10.26165/JUELICH-DATA/8WA9I7). Further inquiries can be directed to the corresponding authors. Users of the simulation code are kindly requested to cite this article.

Author contributions

PY: Conceptualization, Data curation, Formal Analysis, Investigation, Methodology, Validation, Visualization, Writing – original draft, Writing – review and editing. CW: Conceptualization, Data curation, Formal Analysis, Investigation, Software, Validation, Visualization, Writing – original draft, Writing – review and editing. JD: Formal Analysis, Investigation, Methodology, Writing – review and editing. MEP: Investigation, Writing – review and editing. Y-PL: Investigation, Writing – review and editing. DM: Investigation, Writing – review and editing. AK: Funding acquisition, Investigation, Writing – review and editing. RD: Conceptualization, Formal Analysis, Funding acquisition, Project administration, Resources, Supervision, Visualization, Writing – review and editing.

Funding

The author(s) declared that financial support was received for this work and/or its publication. This work was funded by the Federal Ministry of Education and Research project NEUROTEC (Grants No 16ME0398K and No 16ME0399), NeuroSys (03ZU1106AB) and by the Deutsche Forschungsgemeinschaft within TRR 404 Active-3D (Project Number: 528378584). Further funding was received from the Portuguese Foundation of Science and Technology (FCT) through the projects PTDC/08132/2022 (OPERA), LA/P/0037/2020, UIDP/50025/2020 and UIDB/50025/2020 of the Associate Laboratory Institute of Nanostructures, Nanomodelling and Nanofabrication–i3N, as well as from the European Horizon Pathfinder Challenge Program, GA No. 101161114 (ELEGANCE).

Acknowledgments

We would like to thank Grigory Potemkin for doing the top electrode evaporation.

Conflict of interest

The author(s) declared that this work was conducted in the absence of any commercial or financial relationships that could be construed as a potential conflict of interest.

The author RD declared that they were an editorial board member of Frontiers at the time of submission. This had no impact on the peer review process and the final decision.

Generative AI statement

The author(s) declared that generative AI was used in the creation of this manuscript. The authors used ChatGPT (OpenAI, GPT-5.3) solely for language editing and clarity improvement. No AI tools were used for data analysis or generation of scientific content. All content was reviewed and verified by the authors, who take full responsibility for the manuscript.

Any alternative text (alt text) provided alongside figures in this article has been generated by Frontiers with the support of artificial intelligence and reasonable efforts have been made to ensure accuracy, including review by the authors wherever possible. If you identify any issues, please contact us.

Publisher's note

Supplementary material

The Supplementary Material for this article can be found online at: https://www.frontiersin.org/articles/10.3389/fnano.2026.1870683/full#supplementary-material

References

Aussen, S., Cüppers, F., Funck, C., Jo, J., Werner, S., Pratsch, C., et al. (2023). Correlation between electronic structure, microstructure, and switching mode in valence change mechanism Al_2O_3/TiO_x-based memristive devices. *Adv. Electron. Mater.* 9, 2300520. doi: 10.1002/aelm.202300520

Backus, J. (1978). Can programming be liberated from the von neumann style? a functional style and its algebra of programs. *Commun. ACM* 21, 613–641. doi: 10.1145/359576.359579

Baeumer, C., Raab, N., Menke, T., Schmitz, C., Rosezin, R., Müller, P., et al. (2016). Verification of redox-processes as switching and retention failure mechanisms in Nb: $SrTiO_3$/metal devices. *Nanoscale* 8, 13967–13975. doi: 10.1039/c6nr00824k

Bengel, C., Cüppers, F., Payvand, M., Dittmann, R., Waser, R., Hoffmann-Eifert, S., et al. (2021). Utilizing the switching stochasticity of HfO_2/TiO_x-based reram devices and the concept of multiple device synapses for the classification of overlapping and noisy patterns. *Front. Neurosci.* 15, 661856. doi: 10.3389/fnins.2021.661856

Buczek, M., Moos, Z., Gutsche, A., Menzel, S., and Dittmann, R. (2025). $Pr_{1-x}Ca_xMnO_3$-based memristive heterostructures: basic mechanisms and applications. *Chem. Rev.* 125, 6156–6202. doi: 10.1021/acs.chemrev.4c00813

Carvalho, G., Pereira, M., Silva, C., Deuermeier, J., Kiazadeh, A., and Tavares, V. (2022). Characterization and modeling of resistive switching phenomena in IGZO devices. *AIP Adv.* 12, 085017. doi: 10.1063/5.0098145

Chekol, S. A., Menzel, S., Waser, R., and Hoffmann-Eifert, S. (2022). Strategies to control the relaxation kinetics of Ag-based diffusive memristors and implications for device operation. *Adv. Electron. Mater.* 8, 2200549. doi: 10.1002/aelm.202200549

Clemens, W. (2026). *Code repository for band alignment calculations*. Jülich DATA. doi: 10.26165/JUELICH-DATA/8WA9I7

Cooper, D., Baeumer, C., Bernier, N., Marchewka, A., La Torre, C., Dunin-Borkowski, R. E., et al. (2017). Anomalous resistance hysteresis in oxide reram: oxygen evolution and reincorporation revealed by *in situ* TEM. *Adv. Materials* 29, 1700212. doi: 10.1002/adma.201700212

Dittmann, R., Menzel, S., and Waser, R. (2021). Nanoionic memristive phenomena in metal oxides: the valence change mechanism. *Adv. Phys.* 70, 155–349. doi: 10.1080/00018732.2022.2084006

Dobierzewska-Mozrzymas, E., Pieciul, E., Bieganski, P., and Szymczak, G. (2001). Conduction mechanisms in discontinuous Pt films. *Cryst. Res. Technol. J. Exp. Industrial Crystallogr.* 36, 1137–1144. doi: 10.1002/1521-4079(200110)36:8/10<1137::AID-CRAT1137>3.0.CO;2-4

Flynn, B. T., Oleksak, R. P., Thevuthasan, S., and Herman, G. S. (2018). Interfacial chemistry-induced modulation of schottky barrier heights: *in situ* measurements of the Pt–amorphous indium gallium zinc oxide interface using X-ray photoelectron spectroscopy. *ACS Appl. Mater. and Interfaces* 10, 4333–4340. doi: 10.1021/acsami.7b18674

Funck, C., Bäumer, C., Wiefels, S., Hennen, T., Waser, R., Hoffmann-Eifert, S., et al. (2020). Comprehensive model for the electronic transport in $Pt/SrTiO_3$ analog memristive devices. *Phys. Rev. B* 102, 035307. doi: 10.1103/PhysRevB.102.035307

Galloway, E., Armbrüster, M., Kovnir, K., Tikhov, M. S., and Lambert, R. M. (2009). Bromine-promoted PtZn is very effective for the chemoselective hydrogenation of crotonaldehyde. *J. Catal.* 261, 60–65. doi: 10.1016/j.jcat.2008.11.003

Gehring, A., and Selberherr, S. (2006). Tunneling models for semiconductor device simulation. *Handb. Theoretical Computational Nanotechnol.* 10, 469–543.

Greiner, M. T., Helander, M. G., Tang, W.-M., Wang, Z.-B., Qiu, J., and Lu, Z.-H. (2012). Universal energy-level alignment of molecules on metal oxides. *Nat. Mater.* 11, 76–81. doi: 10.1038/nmat3159

Gutsche, A., Siegel, S., Zhang, J., Hambsch, S., and Dittmann, R. (2021). Exploring area-dependent $Pr_{0.7}Ca_{0.3}MnO_3$-based memristive devices as synapses in spiking and artificial neural networks. *Front. Neurosci.* 15, 661261. doi: 10.3389/fnins.2021.661261

Hellwig, J., Funck, C., Siegel, S., Sarantopoulos, A., Spithouris, D., Menzel, S., et al. (2024). Resolving the relaxation of volatile valence change memory. *Adv. Electron. Mater.* 10, 2400062. doi: 10.1002/aelm.202400062

Hu, L., Yang, J., Wang, J., Cheng, P., Chua, L. O., and Zhuge, F. (2021). All-optically controlled memristor for optoelectronic neuromorphic computing. *Adv. Funct. Mater.* 31, 2005582. doi: 10.1002/adfm.202005582

Humood, K., Pan, Y., Reynolds, G., Mughal, M., Wang, S., Serb, A., et al. (2025). Spika: an energy-efficient time-domain hybrid CMOS-RRAM compute-in-memory macro. *Front. Electron.* 6, 1567562. doi: 10.3389/felec.2025.1567562

Huy, H. A., Aradi, B., Frauenheim, T., and Deák, P. (2011). Calculation of carrier-concentration-dependent effective mass in Nb-doped anatase crystals of TiO_2. *Phys. Rev. B* 83, 155201. doi: 10.1103/PhysRevB.83.155201

Ide, K., Nomura, K., Hosono, H., and Kamiya, T. (2019). Electronic defects in amorphous oxide semiconductors: a review. *Physica Status Solidi (A)* 216, 1800372. doi: 10.1002/pssa.201800372

Ielmini, D., and Wong, H.-S. P. (2018). In-memory computing with resistive switching devices. *Nat. Electronics* 1, 333–343. doi: 10.1038/s41928-018-0092-2

Isomura, N., Wu, X., Hirata, H., and Watanabe, Y. (2010). Cluster size dependence of Pt core-level shifts for mass-selected Pt clusters on TiO_2 (110) surfaces. *J. Vac. Sci. and Technol. A* 28, 1141–1144. doi: 10.1116/1.3467033

Kawano, H. (2008). Effective work functions for ionic and electronic emissions from mono- and polycrystalline surfaces. *Prog. Surf. Sci.* 83, 1–165doi. doi: 10.1016/j.progsurf.2007.11.001

Kim, J. Y., Kim, H., Kim, D., and Jang, H. W. (2025). Advancements of amorphous IGZO-based transistors: materials, processing, and devices. *ACS Appl. Electron. Mater.* 7, 4703–4728. doi: 10.1021/acsaelm.5c00605

Klein, A. (2012). Energy band alignment at interfaces of semiconducting oxides: a review of experimental determination using photoelectron spectroscopy and comparison with theoretical predictions by the electron affinity rule, charge neutrality levels, and the common anion rule. *Thin Solid Films* 520, 3721–3728. doi: 10.1016/j.tsf.2011.10.055

Kulikova, D. P., Dobronosova, A. A., Kornienko, V. V., Nechepurenko, I. A., Baburin, A. S., Sergeev, E. V., et al. (2020). Optical properties of tungsten trioxide, palladium, and platinum thin films for functional nanostructures engineering. *Opt. Express* 28, 32049–32060. doi: 10.1364/OE.405403

Le Gallo, M., and Sebastian, A. (2020). An overview of phase-change memory device physics. *J. Phys. D Appl. Phys.* 53, 213002. doi: 10.1088/1361-6463/ab7794

Marot, L., Fleury, J., Haas, D., Iyyakkunnel, S., Sanchez, F., Steiner, R., et al. (2022). *In situ* work function measurements of W, WO_3 nanostructured surfaces. *Surf. Coatings Technol.* 447, 128870. doi: 10.1016/j.surfcoat.2022.128870

Marroun, A., Touhami, N. A., and El Hamadi, T.-E. (2019). "Improved IGZO-TFT structure using high-k gate dielectric materials," in *2019 International Conference on Wireless Technologies, Embedded and Intelligent Systems (WITS)*, 1–4. doi: 10.1109/WITS.2019.8723852

Park, S.-J., Park, S.-R., Jeon, W.-S., Na, J. M., Lim, J. H., Ham, S., et al. (2024). High-quality indium–gallium–zinc oxide films synthesized by atomic layer deposition using a single cocktail precursor based on a liquid-delivery system and their application in transistors and inverters. *J. Mater. Chem. C* 12, 11361–11367. doi: 10.1039/D4TC01843E

Pereira, M. E. (2024). *Optoelectronic Memristive Devices Based on Oxide Semiconductors for the next Generation of Information Technology*. Dissertation: NOVA University of Lisbon.

Pereira, M. E., Deuermeier, J., Figueiredo, C., Santos, A., Carvalho, G., Tavares, V. G., et al. (2022). Flexible active crossbar arrays using amorphous oxide semiconductor technology toward artificial neural networks hardware. *Adv. Electron. Mater.* 8, 2200642. doi: 10.1002/aelm.202200642

Pereira, M. E., Deuermeier, J., Martins, R., Barquinha, P., and Kiazadeh, A. (2024). Unlocking neuromorphic vision: advancements in IGZO-based optoelectronic memristors with visible range sensitivity. *ACS Appl. Electron. Mater.* 6, 5230–5243. doi: 10.1021/acsaelm.4c00752

Polaczek, A., Pekala, M., and Obuszko, Z. (1994). Magnetic susceptibility and thermoelectric power of tungsten intermediary oxides. *J. Phys. Condens. Matter* 6, 7909–7919. doi: 10.1088/0953-8984/6/39/011

Rao, M., Tang, H., Wu, J., Song, W., Zhang, M., Yin, W., et al. (2023). Thousands of conductance levels in memristors integrated on CMOS. *Nature* 615, 823–829. doi: 10.1038/s41586-023-05759-5

Sarantopoulos, A., Waser, R., and Dittmann, R. (2024). Eightwise switching mechanism in memristive $SrTiO_3$ devices and its implications on the device performance. *Physica Status Solidi (A)* 221, 2300483. doi: 10.1002/pssa.202300483

Schultz, T., Vogt, S., Schlupp, P., von Wenckstern, H., Koch, N., and Grundmann, M. (2018). Influence of oxygen deficiency on the rectifying behavior of transparent-semiconducting-oxide–metal interfaces. *Phys. Rev. Appl.* 9, 064001. doi: 10.1103/PhysRevApplied.9.064001

Sebastian, A., Le Gallo, M., Khaddam-Aljameh, R., and Eleftheriou, E. (2020). Memory devices and applications for in-memory computing. *Nat. Nanotechnol.* 15, 529–544. doi: 10.1038/s41565-020-0655-z

Serb, A., Bill, J., Khiat, A., Berdan, R., Legenstein, R., and Prodromakis, T. (2016). Unsupervised learning in probabilistic neural networks with multi-state metal-oxide memristive synapses. *Nat. Communications* 7, 12611. doi: 10.1038/ncomms12611

Shinotsuka, H., Tanuma, S., Powell, C. J., and Penn, D. R. (2015). Calculations of electron inelastic mean free paths. X. data for 41 elemental solids over the 50 eV to 200 keV range with the relativistic full Penn algorithm. *Surf. Interface Analysis* 47, 871–888. doi: 10.1002/sia.5789

Siemon, A., Breuer, T., Aslam, N., Ferch, S., Kim, W., Van Den Hurk, J., et al. (2015). Realization of boolean logic functionality using redox-based memristive devices. *Adv. Functional Materials* 25, 6414–6423. doi: 10.1002/adfm.201500865

Stavroulakis, E., Mavropoulis, A., Fyrigos, I.-A., Rallis, K., Dimitrakis, P., and Sirakoulis, G. C. (2025). "RRAM-based hardware implementation of P systems," in *2025 14th International Conference on Modern Circuits and Systems Technologies (MOCAST)*, 1–4. doi: 10.1109/MOCAST65744.2025.11083961

Sze, S. M., and Ng, K. K. (2006). *Physics of Semiconductor Devices*. 3. John Wiley and Sons.

Takagi, A., Nomura, K., Ohta, H., Yanagi, H., Kamiya, T., Hirano, M., et al. (2005). Carrier transport and electronic structure in amorphous oxide semiconductor, $a\text{-}InGaZnO_4$. *Thin Solid Films* 486, 38–41. doi: 10.1016/j.tsf.2004.11.223

Virtanen, P., Gommers, R., Oliphant, T., Haberland, M., Reddy, T., Cournapeau, D., et al. (2020). SciPy 1.0: fundamental algorithms for scientific computing in python. *Nat. Methods* 17, 261–272. doi: 10.1038/s41592-019-0686-2

Von Neumann, J. (1993). First draft of a report on the EDVAC. *IEEE Ann. Hist. Comput.* 15, 27–75. doi: 10.1109/85.238389

Waldrop, J., Grant, R., Kowalczyk, S., and Kraut, E. (1985). Measurement of semiconductor heterojunction band discontinuities by x-ray photoemission spectroscopy. *J. Vac. Sci. and Technol. A Vac. Surfaces, Films* 3, 835–841. doi: 10.1116/1.573326

Wang, Y. (2025). *Universal Memcomputing in Hardware Realization of Memristive Cellular Nonlinear Networks (Mem^2CNN)*. Dissertation: RWTH Aachen University.

Wang, Y., Schnieders, K., Ntinas, V., Ascoli, A., Cüppers, F., Hoffmann-Eifert, S., et al. (2025). Dynamic analysis of the effect of the device-to-device variability of real-world memristors on the implementation of uncoupled memristive cellular nonlinear networks. *IEEE Trans. Nanotechnol.* 24, 121–128. doi: 10.1109/TNANO.2025.3545251

Waser, R., Dittmann, R., Staikov, G., and Szot, K. (2009). Redox-based resistive switching memories - nanoionic mechanisms, prospects, and challenges. *Adv. Materials Deerf. Beach, Fla.* 21, 2632–2663. doi: 10.1002/adma.200900375

Wilson, J., Zhang, J., Li, Y., Wang, Y., Xin, Q., and Song, A. (2017). Influence of interface inhomogeneities in thin-film schottky diodes. *Appl. Phys. Lett.* 111, 213503. doi: 10.1063/1.5004247

Wulf, W. A., and McKee, S. A. (1995). Hitting the memory wall: implications of the obvious. *ACM SIGARCH Computer Architecture News* 23, 20–24. doi: 10.1145/216585.216588

Xia, Q., and Yang, J. J. (2019). Memristive crossbar arrays for brain-inspired computing. *Nat. Materials* 18, 309–323. doi: 10.1038/s41563-019-0291-x

Yin, X., Battaglia, C., Lin, Y., Chen, K., Hettick, M., Zheng, M., et al. (2014). 19.2% efficient InP heterojunction solar cell with electron-selective TiO_2 contact. *ACS Photonics* 1, 1245–1250. doi: 10.1021/ph500153c

Yin, W.-J., Wen, B., Zhou, C., Selloni, A., and Liu, L.-M. (2018). Excess electrons in reduced rutile and anatase TiO_2. *Surf. Sci. Rep.* 73, 58–82. doi: 10.1016/j.surfrep.2018.02.003

Zhao, J., Liu, J., Sang, L., Liao, M., Coathup, D., Imura, M., et al. (2016). Assembly of a high-dielectric constant thin TiO_x layer directly on H-terminated semiconductor diamond. *Appl. Phys. Lett.* 108, 012105. doi: 10.1063/1.4939650

Zurhelle, A. F., Stehling, W., Waser, R., De Souza, R. A., and Menzel, S. (2022). Oxygen diffusion in platinum electrodes: a molecular dynamics study of the role of extended defects. *Adv. Materials Interfaces* 9, 2101257. doi: 10.1002/admi.202101257